OPEN ACCESS
Journal of Innovative Optical Health Sciences
Vol. 16, No. 4 (2023) 2230012 (19 pages)

DOI: 10.1142/S1793545822300129

World Scientific
www.worldscientific.com

Quantification methodologies on organization and morphology features of fiber-like structures: A review

Chuncheng Wang*,§, Jia Meng*,§, Shuhao Qian*, Lingxi Zhou*, Shenyi Jiang*, Rushan Jiang*, Hantao Zhan*, Xinguo Fang*, Yijie Liu*, Zhihua Ding* and Zhiyi Liu*,†,‡

*State Key Laboratory of Modern Optical Instrumentation
College of Optical Science and Engineering
International Research Center for Advanced Photonics
Zhejiang University
Hangzhou, Zhejiang 310027, P. R. China

†Intelligent Optics & Photonics Research Center
Jiaxing Research Institute
Zhejiang University, Jiaxing, Zhejiang 314000, P. R. China
‡liuzhiyi07@zju.edu.cn

Received 30 May 2022
Revised 24 July 2022
Accepted 24 August 2022
Published 19 October 2022

Among all the structural formations, fiber-like structure is one of the most common modalities in organisms that undertake essential functions. Alterations in spatial organization of fibrous structures can reflect information of physiological and pathological activities, which is of significance in both researches and clinical applications. Hence, the quantification of subtle changes in fiber-like structures is potentially meaningful in studying structure-function relationships, disease progression, carcinoma staging and engineered tissue remodeling. In this study, we examined a wide range of methodologies that quantify organizational and morphological features of fibrous structures, including orientation, alignment, waviness and thickness. Each method was demonstrated with specific applications. Finally, perspectives of future quantification analysis techniques were explored.

Keywords: Biophotonics; orientation; waviness; thickness; fiber-like structure.

1. Introduction

Fiber-like structures are one of the most prevalent ones within biological tissues, playing vital roles in different functions with distinctive morphological features.[1–4] The scale of fibrous structures is widely distributed.[5–9] Tiny fiber-like structures such as

‡Corresponding author.
§These authors contributed equally to this work.

collagen fibers within the extracellular matrix (ECM) and microtubules within cells, whose diameter reaches to microns or even sub-microns,[5,6] respectively, serve as mechanical support,[7] and intracellular conveyance tracks.[8,9] Some cells, such as neurons with axons and dendrites, serving as nerve impulse transmitting pathways, also have fibrous shapes.[10] Vasculatures throughout organism bodies function as substance transportation pipelines, with micron-scale capillaries and meter-scale aortas.[11] These fiber-like structures are all adaptively differentiated in accordance with their functions. Thus, extraction of organizational and morphological features of fiber-like structures in biological organisms can offer abundant information for investigation into structure-function relationship of different tissues, which would be conducive to understanding mechanisms regarding disease initiation and progression.[12–14] Furtherly, identification of subtle changes in abnormal tissues may provide potential biomarkers to assist disease diagnosis and treatment.[5,15–17]

Early recognition of structural features of fibrous tissues was realized by pathologists' manual work on stained pathological sections in clinical applications. The obtained results were generally descriptive and qualitative. Later, some approaches achieved rough quantitative estimations on fibrous tissue organization with statistical recapitulative results. However, these results were often in statistical formation such as probability distribution,[18] which might be insufficient and incompetent to directly reflect the morphological and organizational features at localized regions. With the development of microscopic technologies, such as confocal microscopy, multiphoton excitation fluorescence (MPEF) microscopy, and second harmonic generation (SHG), images with high resolution became available both *ex vivo* and *in vivo*.[19–21] Based on highly resolved microscopic images, there was progress in quantification methods aiming at extracting features of fiber-like structures. Quantification precision was improved by image grid segmentation to a much better level.[22,23] However, relative precision was still not ideal enough and the computational cost was often counterbalanced. At the same time, although three-dimensional (3D) data became readily accessible, quantitative analysis was still mainly limited in a two-dimensional (2D) context, which implied low usage efficiency of acquired datum due to underdeveloped 3D quantification techniques. Besides, some technologies still required manual interactions,[24,25] which led to low degree of automation and sometimes uncertainty. In recent years, there are emerging progressive methods to quantify organizational characteristics of fiber-like structures. In the meantime, a number of parameters have been proposed to quantitatively delineate morphological features with high accuracy.[26–28] With these advances, a more thorough mapping of fiber-like structures with pixel/voxel-wise precision is expected to be achieved.

In this paper, we introduce a wide range of quantification methods to delineate organizational and morphological features of fiber-like structures in biological tissues. We start from the orientation and alignment quantifications since these features are proved to be highly correlated with tissue functions, gene expressions and pathological changes, and emerge as a hot topic in precision medicine in recent years. Then waviness characterization is introduced because waviness is closely associated with the distribution of fiber orientation. Next, we talk about the thickness property which focuses mainly on the morphology of individual fibers. Each feature is unfolded in corresponding application scenarios. Finally, we close with a summary and our perspective on potential future directions.

2. Orientation and Alignment

As mentioned above, fiber-like structures are prevalent in biological tissues, undergoing highly dynamic reorganization in physiological and pathological activities. The orientation of fibrous structures contains massive information about physical activities such as load transferring in tendons,[29] and carcinoma invasion in tissues.[15] Furthermore, quantification methods to extract the orientation distribution can be exerted to offer help for clinical purposes such as disease diagnosis,[30] engineered tissue improvement,[31,32] and wound healing assessment.[33,34] However, previous quantitative analysis typically relied on whole-image processing, such as Fourier Transform (FT) and Hough transform (HT).[32,35–38] Others focused on certain kinds of mathematical computations that respectively based on pixel intensity gradients,[39] the second order derivative matrices,[18,40] and fiber midline tracing.[19] These methods mostly produced

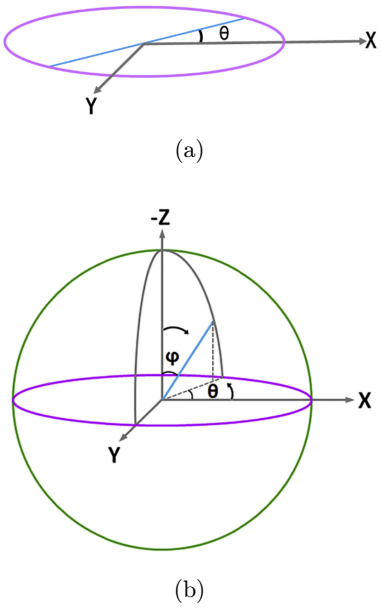

Fig. 1. Definition of orientational angles. Spatial orientation in 2D space with θ (a), and 3D space with θ and φ (b). Reproduced with permission from Ref. 41.

statistical histograms as outputs, instead of direct demonstration at a pixel-wise basis.

Generally, the orientation of fiber-like structures in 2D plane is precisely described by the azimuthal angle, θ, which is in the range from 0° to 180°. As illustrated in Fig. 1(a), θ is defined as the angle between the fiber (blue line) and the x-axis within the plane. When examined in 3D space, an additional polar angle, φ, is needed. As shown in Fig. 1(b),[41] to define the orientation of the fiber (blue line), θ is defined as the angle between the fiber's projection on the xy plane and the x-axis, and the polar angle, φ, is defined as the angle between the fiber and the polar axis, as in this case, the -z axis. Similarly, both θ and φ are within the range between 0° and 180° for axial fiber data. In this manner, a fiber-like structure with arbitrary orientation in space, particularly in 3D space, can be fully determined.[42]

2.1. *Methodologies of orientation and alignment quantification*

2.1.1. *Fourier transform second harmonic generation*

Rao *et al.* performed Fourier transform second harmonic generation (FT-SHG) imaging and quantitative analysis on collagen fibers in different porcine organs.[43] This measurement started with the 2D Fourier transform (2D FT) results from certain regions of interest (ROIs) of SHG images. Typically, high intensity frequencies in the FT spectrum had preferred orientation, which in general was perpendicular to the preferred orientation that collagen fibers aligned with. Next, the 2D FT results, or the extracted FT spectrums, were then binarized by amplitude thresholding to make the dominant spatial frequencies stand out. A raw SHG collagen fiber image and three ROIs along with corresponding binarized FT spectra are shown in Fig. 2(a).[43] Furthermore, the binarized spectrum could be processed with proper fitting to extract the randomness of fiber organization in real space.

2.1.2. *2D and 3D weighted vector summation*

Quinn *et al.* developed a 2D fiber orientation quantification method called weighted vector summation algorithm to map the pixel-specific distribution of azimuthal angle, with corresponding schematic and related formulas shown in Fig. 2(b).[44] In general, this algorithm operated based on analysis of the variation of pixel intensities. A square window (shown in Fig. 2(b),[44] left column) was first generated with all possible symmetric vectors passing through the center pixel. Second, each vector was weighted by two factors, W_1 and W_2, as indicated by the equations in Fig. 2(b).[44] The factor W_1 was defined as the inverse of a vector's length so that all vectors contributed equally in the calculation of orientation for the center pixel. The other factor, W_2, was relevant to the intensity variation along the vector, so that vectors with more uniform intensity weighted heavier. Next, all weighted vectors were summed up to obtain the average orientation of the center pixel, as shown in the lower right corner in Fig. 2(b).[44] After calculating all pixels with respective corresponding windows, a new matrix with pixel-wise azimuthal angle was produced. Following this, Liu *et al.* extended the 2D weighted vector summation algorithm to 3D scale and proved the superiority of 3D methodology by simulation and experimentation.[45] As elucidated above, 3D orientation was defined by the azimuthal angle, θ, and polar angle, φ. The polar angle was typically difficult to calculate. In this context, two extra angles, γ and β, were introduced in the way similar to θ, with γ defined as the angle between the fiber's projection in the yz plane and the y axis, and β defined as the

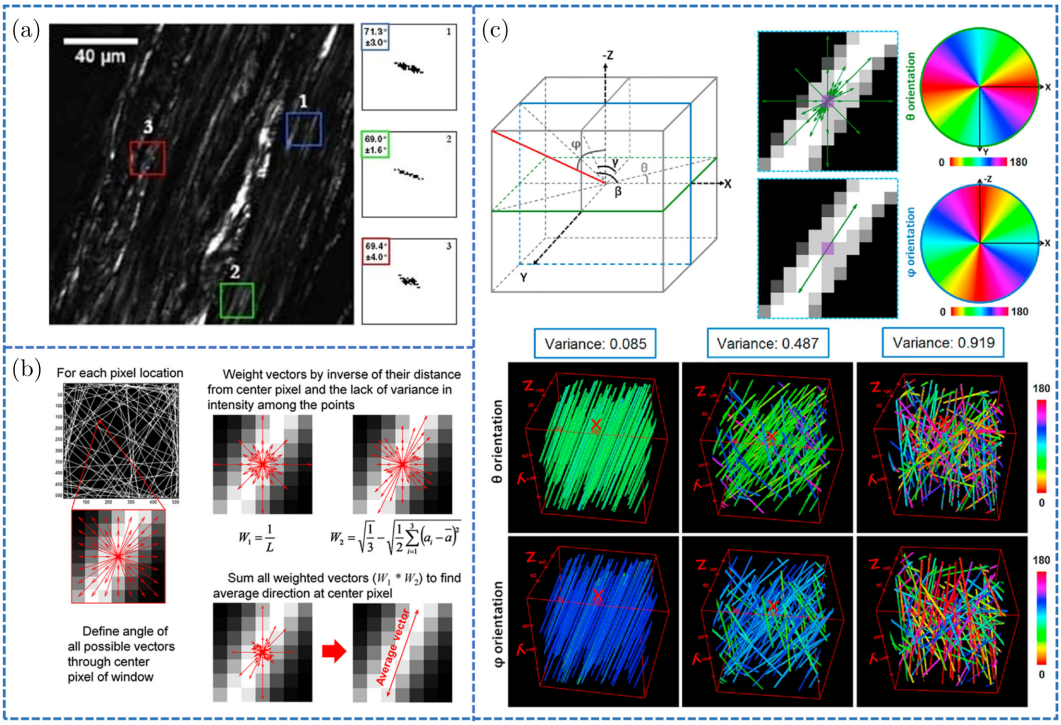

Fig. 2. Schematic representations of orientation and alignment quantification methods. (a) FT-SHG of raw porcine ear image. FT analysis results indicate preferred collagen fiber orientation at three distinct regions. (b) Schematic of 2D weighted vector summation algorithm. (c) Schematic of 3D weighted vector summation algorithm and the resultant alignment metric, 3D directional variance. Three examples of fiber stack with distinct fiber alignment were simulated to test the ability of the 3D directional variance metric. Reproduced with permission from Refs. 43, 44 and 45, respectively.

angle between the fiber's projection in the zx plane and the x axis [Fig. 2(c)].[26] With the extraction of these two extra angles, γ and β, the polar angle φ could be extracted by the equation

$$\tan^2\varphi = \frac{1}{\tan^2\gamma} + \frac{1}{\tan^2\beta}. \tag{1}$$

In this way, a 3D matrix depicting voxel-wise fiber orientation in 3D place was generated, which was then followed by a color-code procedure to enhance degree of visualization. The output orientation maps of θ and φ at two specific planes were illustrated in Fig. 2(c), upper right.[26] Moreover, Liu *et al.* defined a new normalized parameter called 3D directional variance, V_{3D}, based on the 3D orientation results to describe the alignment of fiber-like structures, as calculated by the following equations:

$$V_{3D} = 1 - \bar{R}_{3D}, \tag{2}$$

$$\bar{R}_{3D} = \sqrt{\bar{C}_{3D}^{a2} + \bar{S}_{3D}^{a2} + \bar{Z}_{3D}^{a2}}, \tag{3}$$

where the superscript a indicates the fibrillar axial data. Specially, if it was defined as: $b_j = \sqrt{1/\tan^2(2\beta_j) + 1/\tan^2(2\gamma_j)}$, then the calculation can be proceeded by

$$\bar{C}_{3D}^{a} = (1/n)\sum_{j=1}^{n}(b_j/\sqrt{1+b_j^2})\cos(2\theta_j), \tag{4}$$

$$\bar{S}_{3D}^{a} = (1/n)\sum_{j=1}^{n}(b_j/\sqrt{1+b_j^2})\sin(2\theta_j), \tag{5}$$

$$\bar{Z}_{3D}^{a} = (1/n)\sum_{j=1}^{n} SI/\sqrt{1+b_j^2}, \tag{6}$$

$$SI = \begin{cases} (-1)\cdot(\varphi - 90^\circ)/|\varphi - 90^\circ|, & \text{when } \varphi \neq 90^\circ \\ 1, & \text{when } \varphi = 90^\circ \end{cases}, \tag{7}$$

where n indicates the total number of voxels devoted to the calculation of 3D directional variance. Specifically, the variance value was close to 0 when fibers were parallel to each other, while it approached 1 when fibers distributed randomly. Simulated fiber stacks with low, intermediate and high fiber alignment are shown in Fig. 2(c), bottom.[26] The 3D directional variance metric was proved to be robust and competent in alignment quantification of fibrillar structures in 3D context.[26]

2.1.3. *Diffusion tensor magnetic resonance imaging*

Magnetic resonance imaging (MRI), based on signals from proton nuclei, was a commonly used technology in both neurological science and clinical diagnosis. The traditional MR signal was usually acquired by:

$$S = PD(1 - e^{-TR/T_1})e^{-TE/T_2}e^{-bD}, \tag{8}$$

where PD is the proton density, T_1 and T_2 are signal relaxation times after excitation relating to the environment, D is the diffusion term indicating water molecules' Brownian motion, TR and TE are related to the excitation (time of repetition) and preparation period (time of echo) and b is the diffusion-weighting factor. Specifically, the last three parameters were controllable.[46] However, this technology was typically limited in both spatial resolution and contrast. In order to address this issue, the diffusion tensor magnetic resonance imaging (DT-MRI), or diffusion tensor imaging (DTI), was introduced as a promising tool.[46] The principle of DTI was based on the self-diffusion property of water molecule, as indicated by the diffusion term, D, in Eq. (8). In general, the diffusion was anisotropic in the surrounding area of white matter fiber bundles, since water molecules moved more easily along the axonal bundles rather than perpendicular to these bundles, which resulted in a set of water self-diffusion coefficients, D, that could be determined by sensitized MR signal.[47] In order to extract D to reflect fiber orientation information, two images with the same parameter values but different b were required, as expressed by the following equations[46]:

$$S_1 = PD(1 - e^{-TR/T_1})e^{-TE/T_2}e^{-b_1D} = S_0e^{-b_1D}, \tag{9}$$

$$S_2 = S_0e^{-b_2D}, \tag{10}$$

$$\frac{S_2}{S_1} = e^{-(b_2-b_1)D}, \tag{11}$$

$$D = -\ln\left(\frac{S_2}{S_1}\right) \Big/ (b_2 - b_1), \tag{12}$$

where S_1 and S_2 are signal intensities with different b parameters. Thus D, the diffusion coefficient, was derived from the two intensities with constant PD, TR and TE parameters. A gradient pulse along a coordinate axis was applied to induce phase differences among molecules located along the gradient axis within a pulse period, from which the water motion could be deduced. According to Eq. (8), a higher diffusion coefficient, D, implies more signal loss, which could be manipulated by extending the interval between two pulses or adjusting the strength of the pulse. By manipulating b, a non-diffusion-weighted image S_1 and a diffusion-weighted image S_2 were obtained. Next, by solving Eqs. (11) and (12), an apparent diffusion coefficient (ADC) map was acquired. The ADC maps were finally obtained in the three coordinate axes (X, Y and Z). Since fiber orientations are often at an angle to the axis, Basser *et al.* introduced the effective diffusion tensor, D_{eff}, and the fitted diffusion ellipsoid model, to better quantify and describe the diffusion property of the fibers.[48] The axis-measured-data fitted ellipsoid could represent average diffusion range in each direction, with the length of the longest, middle and shortest axes called eigenvalues λ_1, λ_2, and λ_3, and respective orientations called eigenvectors v_1, v_2, and v_3, altogether six parameters.[46] Furthermore, a 3×3 symmetric tensor was utilized to transform ADC maps into the six parameters. With these results, a new metric, fractional anisotropy (FA) was defined to characterize diffusion anisotropy:

$$FA = \sqrt{\frac{1}{2}}\frac{\sqrt{(\lambda_1 - \lambda_2)^2 + (\lambda_2 - \lambda_3)^2 + (\lambda_3 - \lambda_1)^2}}{\sqrt{\lambda_1^2 + \lambda_2^2 + \lambda_3^2}}. \tag{13}$$

The FA value ranged from 0 (isotropic) to 1 (anisotropic), indicating the fiber alignment degree. The acquired FA map could be visualized with a gray-scale coding [Fig. 3(a)]. Meanwhile, the 3D fiber orientation information could be reduced to the direction of v_1 and a color-coded orientation map could then be generated accordingly [Figs. 3(b) and 3(c)].

2.1.4. *3D-polarized light imaging method*

Markus *et al.* came up with a 3D-polarized light imaging (3D-PLI) to quantify the 3D orientation of fiber tracts in human brain based on the inherent birefringence property of myelin sheath outside the axon.[49] First, the human brain sections were imaged by a constructed polarimeter, which was composed of two orthogonal linear polarizers, a $\lambda/4$ phase retarder sandwiched between polarizers and a specimen stage. The scanning of images with a sequence of discrete angles was conducted by rotating

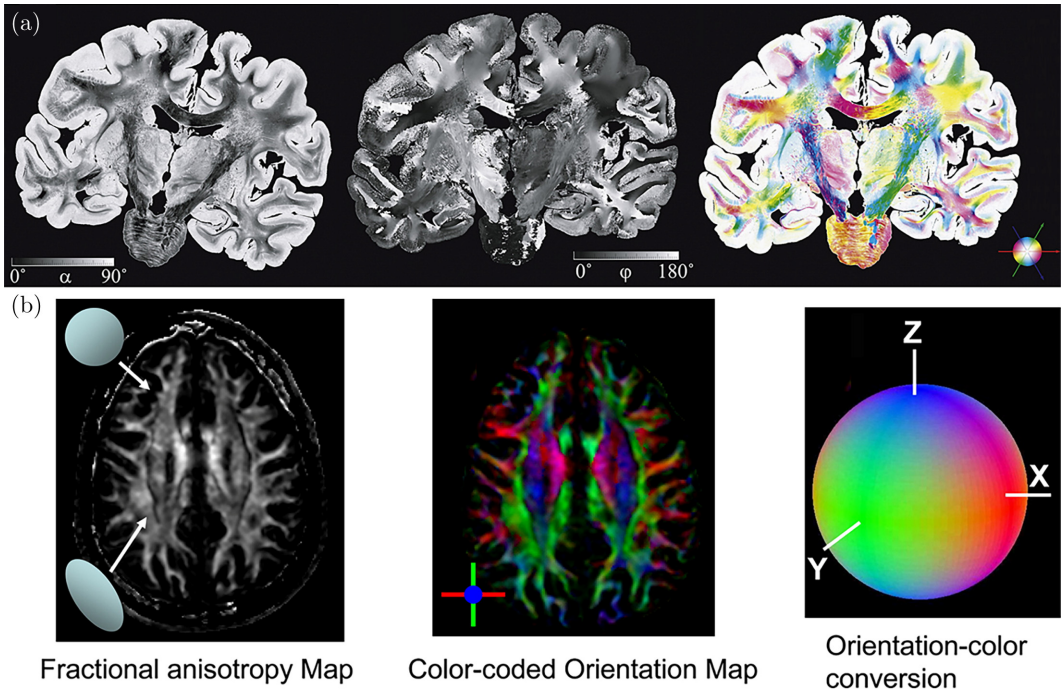

Fig. 3. Demonstration of diffusion tensor imaging (DTI, or DT-MRI) and 3D-polarized light imaging (3D-DLI) quantification methods. (a) Fractional anisotropy (FA) map of cerebral fiber tracts. (b) Color-coded 3D orientation map of cerebral fiber tracts. (c) 3D orientation color conversion legend of (b). (d) Grayscale encoding polar angle (inclination) map of brain section. (e) Grayscale encoding azimuthal angle (direction) map of brain section. (f) HSV color-coded orientation map integrating both inclination and direction information, with the color sphere at the corner as a legend. Reproduced with permission from Refs. 46 and 49.

the optical system around the stationary sample, as PLI raw images, for each brain section. Owing to the complete polarized light system, Jones calculus was applied to calculate the transmittance through the polarimeter. Thus, the light intensity, I, was obtained at the pixel level with the following expression:

$$I = \frac{I_0}{2} \cdot [1 + \sin(2\rho - 2\theta) \cdot \sin(\delta)], \tag{14}$$

where I_0 indicates the incident light affected by local extinction effects, ρ indicates the azimuth of the transmission axis of the first polarizer, θ denotes the azimuthal angle introduced in Fig. 1(b),[41] and δ indicates the phase retardation due to the myelin, which could be further calculated by the equation below:

$$\delta \approx 2\pi \cdot \frac{d \cdot \Delta n}{\lambda} \cdot \cos^2\varphi, \tag{15}$$

where λ denotes the wavelength, d denotes the section thickness, Δn denotes the birefringence effect and φ denotes the polar angle introduced in Fig. 1(b).[41] As introduced previously, θ and φ were able to depict a certain orientation of fibers in 3D space. In practice, the PLI intensity profiles required a three-step pre-processing to remove the impact of absorption, scatter and noise: image calibration, non-target segmentation and removal, and spatial independent component analysis (ICA). After pre-processing, discrete harmonic Fourier analysis was applied to the amended profiles, so that the light intensity, I, was parameterized as

$$I = a_0 + a_1 \cdot \sin(2\rho) + b_1 \cdot \cos(2\rho), \tag{16}$$

$$a_0 = \frac{I_0}{2} = \frac{1}{N}\sum_{i=1}^{N} I_i, \tag{17}$$

$$a_1 = \frac{I_0}{2} \cdot \sin\delta \cdot \cos(2\theta) = \frac{2}{N}\sum_{i=1}^{N} I_i \cdot \sin(2\rho_i), \tag{18}$$

$$b_1 = -\frac{I_0}{2} \cdot \sin\delta \cdot \sin(2\theta) = \frac{2}{N}\sum_{i=1}^{N} I_i \cdot \cos(2\rho_i), \tag{19}$$

where I_i indicates the light intensity in accordance to the rotation angle ρ_i and N indicates the total number of sampled data points, i. In the next step, θ and φ were quantified. The fiber inclination map depicted by the polar angle φ was calculated by

combining the following expressions:

$$|\sin\delta| = \left|\sin\left(\frac{\pi}{2}\cdot d_{\text{rel}}\cdot\cos^2\varphi\right)\right|, \tag{20}$$

$$|\sin\delta| = \sqrt{a_1^2+b_1^2}/a_0, \tag{21}$$

where d_{rel} indicates the ratio of the actual section thickness d to the ideal thickness $d_{\lambda/4}$ which causes $\pi/2$ phase retardation, reflecting relative thickness of the section. The direction map depicted by the azimuthal angle θ was acquired from fit functions, which was determined at the minimum while fitting the intensity profile. Finally, after proper registration procedures, the fiber inclination map [Fig. 3(d)] and direction map [Fig. 3(e)] could be visualized, which were further combined to generate a volume fiber orientation map [3D-FOM, Fig. 3(f)].

2.1.5. *ImageJ and CT-FIRE methods*

In recent years, some automatic and semi-automatic methods become available as free-source tools for quantification of fiber orientation and alignment. Bredfeldt *et al.* combined the curvelet-transform (CT) based denoising filter and a tracking algorithm called fiber-extraction (FIRE) together, as CT-FIRE, which had potential in collecting multiple physical features of collagen fibers such as length, curvature, number and orientation.[50] First, images were preprocessed with filters to enhance fringe information and depress noise. Then the FIRE algorithm was applied to processed images for the extraction of the fiber trajectory.[51] Specifically, images were applied threshold during the preprocessing to produce a binary mask to distinguish collagen from the background. After that, the distance transform was performed on the collagen pixels to calculate the nearest distances from the background. Next, a set of nucleation points were made from the trace of ridgeline of the transformed image, from which branches were extended. Finally, the fiber trajectory was identified by connecting adjacent fibers while omitting negligible fibers. Venter *et al.* further combined ImageJ and CT-FIRE method to measure the orientation of muscle cells with alignment index (AI).[52] At the very beginning, they validated the method's adaptability and feasibility in quantifying the orientation of elliptical shapes (in this case, myoblasts) with simulation since the CT-FIRE method was originally developed targeting at linear collagen fibers. Then, images were binarized adaptively with the help of ImageJ, with an order of grayscale conversion, noise removal and local thresholding.[53] Next, these binarized images were processed with CT-FIRE algorithm to calculate AI. Particularly, the authors found that the calculation of AI should use the preferred orientation (the average value of cell orientations with maximal frequency range values) rather than the average orientation (the average value of total orientations) with the following equation:

$$AI = \frac{1}{N}\sum_{i=1}^{N}(2[\cos(x-y)]^2-1), \tag{22}$$

where N stands for the total number of quantified cells, x is the preferred orientation (ranging from 0° to 180°), and y is the orientation of a standalone muscle cell. The AI value ranged between 0 and 1, where disorderly scattered cells with a value drawing near to 0 and aligned cells with a value close to 1.

2.2. *Applications of orientation and alignment quantification*

Regarding the application of orientation and alignment algorithms, Sivaguru *et al.* utilized the ROI-scale 2D FT-SHG technique together with histogram analysis to quantitatively identify more aligned collagen fibers in normal than injured horse tendons. The conclusion that FT-SHG method performed better than previously used polarization microscopy with enhanced sensitivity was also derived.[22] Ambekar *et al.* also conducted similar quantification method on porcine bones and concluded that collagen fibers became more organized as bone aged.[23] Later, in order to extract organizational features of collagen fibers, this group defined fraction of anisotropic region number to the isotropic region number as anisotropic to isotropic ($A.I.$) ratio based on FT power spectrum analysis, and used this metric to distinguish malignant breast tumors from those of other stages.[54] Although 2D FT-SHG methods were effective in quantitatively depicting fiber orientation at ROI scale, there was still a tradeoff between computational cost and precision. Meanwhile, 2D methods were less competent in quantifying collagen fibers that stacked up and aligned across optical sections.

Lau *et al.* used the FT-SHG imaging to assess collagen fiber organization in mouse cervices.[55]

In particular, the acquired images were analyzed with both 2D and 3D FT. First, images were gridded so that orientation of fibers in each region could be properly described. Then regions with negligible signals were labeled to be dark. Next, regions whose frequency spectrum possessed obvious peaks were referred to as anisotropic and the corresponding preferred orientation was allocated, similar to the analysis performed by Rao *et al.*,[43] whereas regions in lack of obvious peaks in spectrum were tagged as isotropic. In this way, a ternary-label map with isotropic regions marked with preferential orientations was generated. The raw 2D SHG image and corresponding ternary-label map, with two representative 3D reconstructed areas, are shown in Fig. 4(a).[55] Additionally, this group performed similar methods to quantify collagen fiber organization in porcine sclera and concluded that collagen fibers aligned consistently within a certain layer while variously among different layers.[56] By comparison, the 3D FT analysis was more sensitive than the 2D counterpart in quantifying the orientation of non-negligible quantities of collagen fiber that aligned obliquely to optical sections. Meanwhile, the 3D method was also advantageous in quantifying orientation variation of interlayer collagen fibers. However, the problem of grid size determination still existed.

Quinn *et al.* utilized their algorithm to map the pixel-specific orientation distribution of several kinds of distinct fiber-like structures with different imaging methods, as shown in Fig. 4(b).[44] These

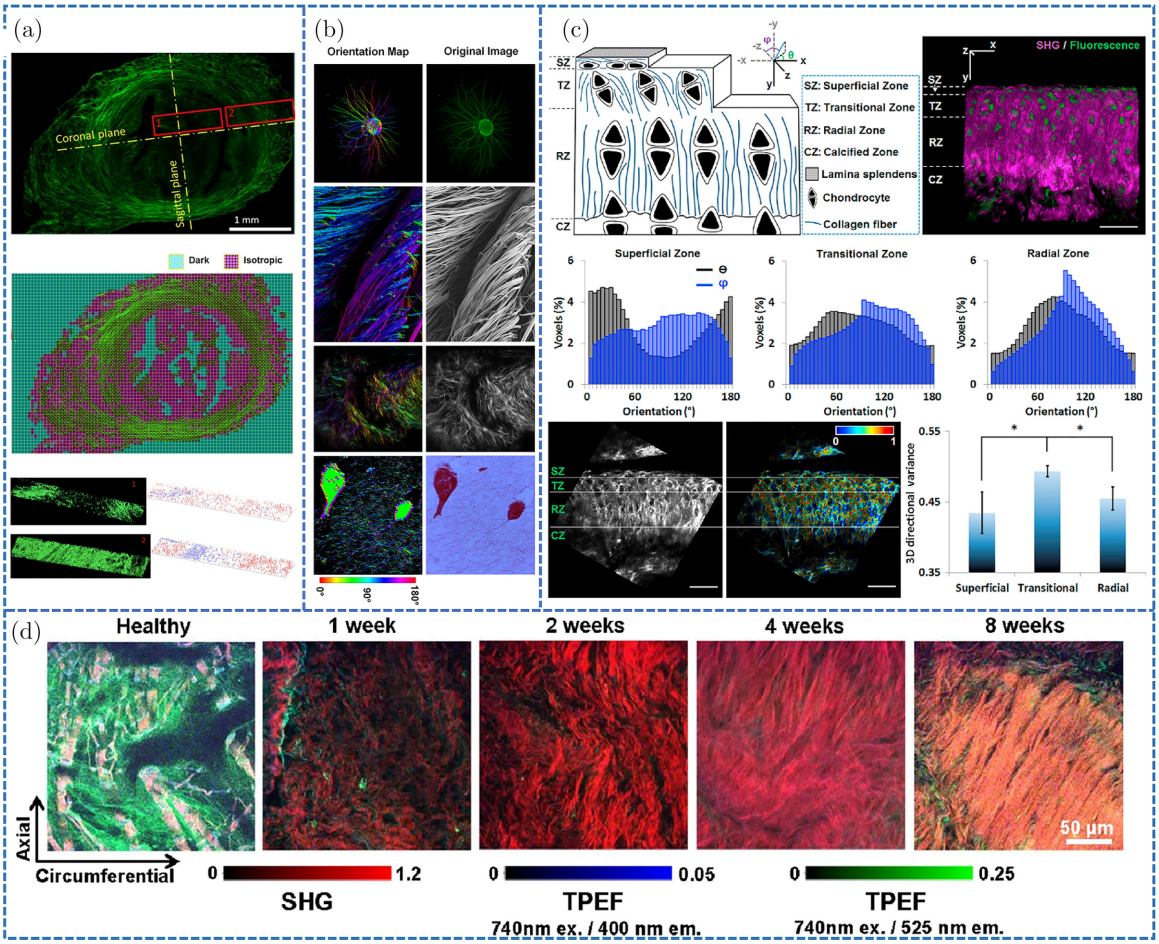

Fig. 4. Application examples of distinctive orientation quantification methods. (a) The raw SHG image and corresponding ternary-label map acquired from 3D FT-SHG analysis, along with 3D rendered models of raw images and ROI-level preferred orientation distribution of two regions 1 and 2. (b) Raw images and 2D orientation maps of neurites, silk fibers, collagen and MCF10A cell cultures, acquired from 2D vector summation algorithm. (c) 3D vector summation and directional variance algorithm applied in modeling and distinguishing different layers of mouse articular cartilage. *, $p < 0.05$; Scale bar, 50 μm. (d) Quantitative images of both collagen fibers and crosslinks from the heart tissue at different time points following heart infarction. Reproduced with permission from Refs. 14, 26, 44 and 55.

fiber-like structures included neurites, silk fibers, and collagen fibers within tissues and MCF10A cell cultures. As can be seen, the quantification results exhibited excellent consistence with raw images from different imaging modalities, which fully proved the robustness of the algorithm. After extension to 3D format, the 3D weighted vector summation algorithm and 3D orientation variance parameter were applied by Liu *et al.* to modeling the physical structure of mouse articular cartilage.[26] The schematic model, 3D reconstructed multi-photon microscopy images, typical orientation histograms and 3D directional variance analysis results are shown in Fig. 4(c).[26] The articular cartilage model contained four layers from the inside to outside: calcified, radial, transitional and superficial zones.[26] Furthermore, orientation histograms implied that fibers in the radial zone tended to align perpendicular to the articular surface, while fibers in the superficial zone preferred to orient parallel to the surface. Yet in the transitional zone, fibers distributed more broadly in orientation. Further, 3D directional variance analysis results [last row in Fig. 4(c)] indicated that collagen fibers in the radial and superficial zone were more aligned than those in the transitional zone, in accordance with the orientation histograms.[26] This algorithm with relevant variance parameter has been proved to be competent in mapping voxel-wise orientational and organizational distributions of collagen fibers in the articular cartilage model.

The orientation and alignment of collagen fibers were closely associated with the way and extent of cross-linking, which referred to the ability of collagen fibrils to form strong chemical bonds with adjacent fibrils.[57] Cross-linking functions in collagen organization modulation, stromal stiffness variation, and can be responsible for ECM remodeling alteration, some of which may be contributed to gene regulation.[58] Moreover, cross-linking was correlated with the autofluorescence of collagen fibers.[59] In terms of quantification, Marturano *et al.* proved that the two-photon excitation fluorescence (TPEF) signal at certain excitation-emission settings was sensitive to cross-linking, as validated by the traditional liquid chromatography-mass spectrometry measurements.[60] This implicated a quantitative imaging method to identify cross-linking within collagen fibers. Based on this clue, Quinn *et al.* excited cross-linking with 740 nm laser and gathered the TPEF autofluorescence emission signal at the wavelength of both 400 nm and 525 nm [Fig. 4(d)].[14] Quantitative analysis indicated that increased cross-linking level, as represented by the enhanced TPEF signal intensity, was positively interrelated to the increased alignment of collagen fiber (i.e., decreased 3D directional variance) while recovering from mice heart infarction.

3. Waviness

Among various parameters for morphological features of fiber-like structures, waviness was an important one since the variation of which was easily subject to load and stress. The degree of waviness (or curvature, undulation, tortuosity) of fibrillar structures, W, was often related to the ratio of the chord length to the arc length, which was also referred to as *straightness parameter*.[61] This quantification parameter was successfully utilized to study the stress-loaded structural variation of blood vessels, such as stiffness difference in distal and proximal regions of thoracic and abdominal porcine aorta,[62,63] reaction in the medial layer of ovine pulmonary artery wall,[64] and uncrimping process in primate artery.[24] Moreover, waviness of elastic laminas (ELs) in both circumferential and longitudinal directions was measured to deduct the buckling structure of ELs.[65] In addition, morphological abnormalities of collagen fibers in ECM may provide information about pathological changes. For example, the waviness of partial collagen fibrils in abdominal aortic aneurysms was characterized to be abnormally increasing.[66]

3.1. *Methodologies of waviness quantification*

3.1.1. *Descriptive parameter aspect ratio*

Benboujja and Hartnick provided a plain description on continuous collagen fibers while examining human vocal fold structures in the anterior region.[67] As can be seen from the 3D reconstruction of combined TPEF and SHG images [top, Fig. 5(a)],[67] elastin (red) and collagen fibers (green) exhibited a quasi-sinusoidal wave-like pattern. This waviness shape could be delineated as peaks and valleys with a *spatial period* value, λ, and an *amplitude* value, a [bottom, Fig. 5(a)]. A similar metric, aspect ratio, was also defined as the ratio of a and λ to describe marcel in glass fiber composites.[68] However, this

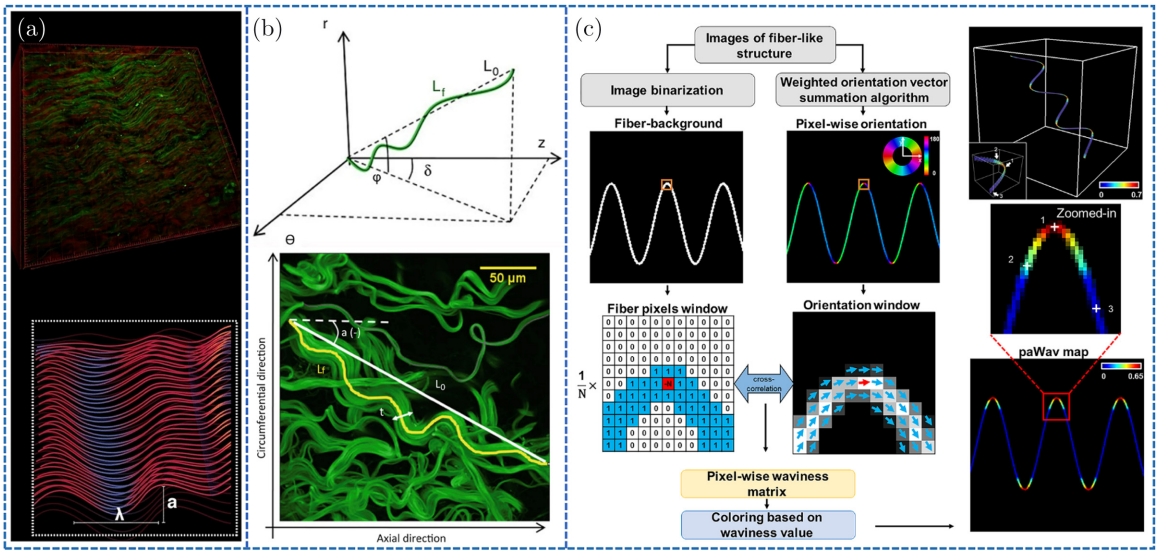

Fig. 5. Schematics of waviness quantification methods. (a) 3D rendering of elastin and collagen fibers in human vocal fold, with the inset showing fibers exhibiting quasi-sinusoidal wavery linear shapes and described by two parameters. (b) Schematics showing definition of *straightness parameter* in 3D and 2D spaces. (c) Flowchart showing the process of calculating *paWav* distribution and post-mapping illustration. Reproduced with permission from Refs. 28, 61 and 67.

metric was not widely applicable since most fiber shapes were far from firmly sinusoidal structure.

3.1.2. *NeuronJ based straightness parameter quantification*

Rezakhaniha *et al.* put forward *straightness parameter* to quantify the collagen fiber waviness in arterial adventitia imaged by confocal microscopy.[61] As can be seen from Fig. 5(b),[61] the *straightness parameter* (P_s) was defined by the following expression:

$$P_s = L_0/L_f, \tag{23}$$

where L_0 represented the straight line distance between two ends of the examined fiber bundle and L_f represents its actual length. The P_s value is distributed within the range between 0 and 1, with a completely straight fiber drawing near to 1 and a highly-wavy fiber approaching 0. In other words, this metric could mediately reflect the degree of waviness. In order to acquire L_0 and L_f, an ImageJ plug-in, NeuronJ, was utilized to quantify collagen fibers within 2D images manually.

3.1.3. *Pixel-wise automated waviness quantification*

Recently, Qian *et al.* reported another normalized metric, the *pixel-wise, automated waviness (paWav)*, to quantify morphology of fiber-like structures, with a lower value representing straighter fibers.[28] As can be seen from Fig. 5(c),[28] the algorithm was based on pixel-wise orientation matrix and corresponding binarized mask, which were outputs from weighted orientation vector summation algorithm.[44,45] First, an m × m pixel window was generated and centered at each fibrillar pixel (pixels with value 1 in the binarized mask) in both orientation matrix and binary mask. For the binary mask, the pixel value at window center was modified as $-N$, where $N+1$ represented fibrillar pixel number within the window, and then each pixel value in the window was divided by N. Next, the two windows from separate matrices were performed with cross-correlation which averaged the summation of orientation difference between all non-centered pixel and the center pixel value within the window. Next, the operation result was followed by division of 90 as normalization. Finally, a new matrix formed by normalized values from all windows was color-coded to generate the pixel-wise waviness map.

3.2. *Applications of waviness quantification*

Regarding applications of waviness quantification algorithms, Rezakhaniha *et al.* quantified collagen fiber straightness distribution of carotid artery

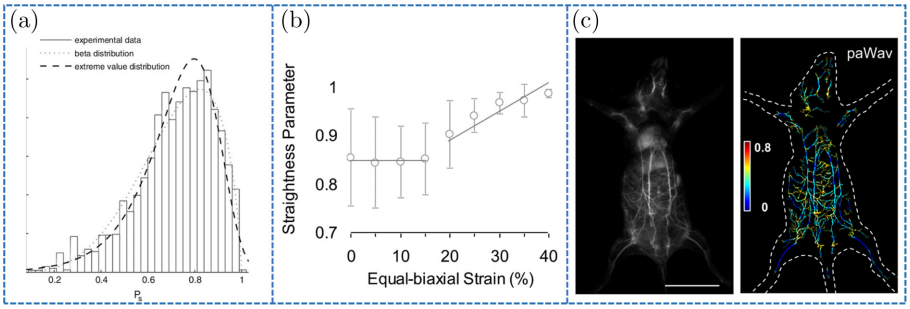

Fig. 6. Applications of waviness quantification algorithms. (a) Weighted *straightness parameter* histogram distributions of rabbit carotid artery adventitia fibers, fitted by beta and extreme value distribution methods. (b) *Straightness parameter* of porcine thoracic aortas adventitial collagen fibers responding to equal-biaxial strain. (c) Raw image and color-coded *paWav* distribution map of whole-body blood vessels in mouse. Scale bar: 15 mm. Reproduced with permission from Refs. 28, 61 and 69.

adventitia in rabbits.[61] With the help of NeuronJ, the *straightness parameter* (P_s) datum was extracted and its probability density distribution was fitted by beta and extreme value distributions, as shown in Fig. 6(a).[61] As a result, beta distribution performed better for zero-stress straightness of collagen fibers in adventitia, which was also confirmed by other similar studies.[42] This quantification method was able to determine straightness distribution type, offering information to explore inner structure of collagen fiber in adventitia. Chow *et al.* also quantified the waviness changes of elastin and collagen fibers in porcine thoracic aortas adventitia during mechanical loading by P_s with NeuronJ.[69] The change of P_s with increasing biaxial strain is plotted in Fig. 6(b),[69] with x-axial variable defined as $(l - L)/L$, where l and L were original and resultant length of the target. This plot indicated that strain higher than 20% significantly increased the P_s of collagen fibers, which was in accordance with former conclusion that collagen fibers turned to be the main load bearing structure at higher tension.[70] Chen *et al.* extended the fiber-stretch study with P_s on coronary adventitia and concluded that most collagen fibers would straighten when $(l - L)/L$ reached 80%.[71] Although the *straightness parameter* has been successfully utilized as a metric to quantify crimpy degree of fiber-like structures, presentation approaches were limited to statistical diagrams and/or line charts, which lacked intuitiveness. And the extraction process of P_s typically required extra manual operation.

Qian *et al.* applied their algorithm to studying waviness variation during microtubule-associated endoplasmic reticulum (ER) formation process from time-dependent super-resolution images acquired by structured illumination microscopy (SIM).[27] With the help of extracted dynamic waviness changes in color-coded map in combination with orientation assessments, a new microtubule-associated ER formation mechanism, termed hooking, was identified, in addition to the three mechanisms recognized already. Later, Qian *et al.* utilized their algorithm to map pixel-wise waviness distribution of the whole-body blood vessels in mice, based on aggregation-induced emission luminogens (AIEgens) excited fluorescence images.[28] A typical raw image and corresponding color-coded *paWav* map are shown in Fig. 6(c).[28] The algorithm proposed by Qian *et al.* successfully depicted the waviness distribution of fiber-like structures ranging from subcellular microtubules to large-scale whole-body vessels automatically at pixel-level accuracy. Meanwhile, the color-coded output provided direct visualization of wavy features, which might enable a better understanding of morphological alterations in physiological and pathological activities.

4. Thickness

Vascular structures and systems were basic fiber-like structures in mammal bodies and played an important role in substance delivering. Thus, morphological variations in vasculature, particularly in blood-vascular system, were related to anomalies concerning pathological changes such as tumor growth,[72] cerebral injuries,[73] cardiovascular anomalies,[74] and ophthalmic diseases.[75] Compared with other fiber-like structures, blood vessels were larger in size. In this way, the thickness of vessel was regarded as a significant feature since its variation could reflect changes in pulse wave velocity,[76] blood

pressure,[77,78] and even body mass index (BMI).[79] For instance, children with higher blood pressure were more likely to possess thinner retinal arteriolar calibers than those with lower blood pressure.[79,80] Nevertheless, attention was mainly focused on studying the relationship between vessel diameters and other heath indexes through statistical analysis, while little has been paid to a direct visualization of thickness changes.

4.1. *Methodologies of thickness quantification*

4.1.1. *Improved boundary intersection method*

For 2D vessel thickness quantification, the method of calculating distance between two vessel edges was commonly applied [top, Fig. 7(a)].[81] While in 3D images, vessels were reconstructed to be cylindrical structures, where the distance between edge points was not appropriate to represent their diameters. To improve this shortcoming of the 2D method, Sun *et al.* proposed the 3D boundary intersection method to quantify the blood vessel diameter based on photoacoustic images [bottom, Fig. 7(a)].[81] The vessel skeleton line and edges were first extracted. Then, a circle perpendicular to the skeleton line with finite points was fitted to the vessel perimeter. Next, the circle's radius was increased with finite points so that sufficient perimeter points would intersect with the vessel edges. Finally, the distances between each perimeter point and the circle center were averaged to estimate the vessel diameter. The robustness of extended 3D approach was affirmed by a test on tungsten wire measurement which showed superior accuracy over 2D method.

4.1.2. *Gradient-guided minimum radial distance algorithm*

Wei *et al.* put forward a gradient-guided minimum radial distance (MRD) algorithm to quantify blood vessel diameter,[82] as shown in Fig. 7(b). The original simulated vascular structure image was first binarized by thresholding and filtering. Then the binary map was converted to a one-pixel-wide skeletonized map, or vessel skeleton map (*VSM*) by iterative boundary corrosion and a vessel perimeter map (*VPM*) by edge detection, respectively. Next, the minimal distances from the skeleton to both opposite perimeters were calculated. Finally, the diameter value corresponding to the skeleton pixel was estimated by the summation of two related distance values offered by the last step, with the expression below

$$D = \min_{i \in VPM, Q} \left(\sqrt{(x_i - x)^2 + (y_i - y)^2}\right) + \min_{j \in VPM, \bar{Q}} \left(\sqrt{(x_i - x)^2 + (y_i - y)^2}\right), \quad (24)$$

where D indicates the vessel's diameter, (x, y) indicates the coordinate of a pixel at the extracted skeleton, (x_i, y_i) and (x_j, y_j) indicate coordinates of

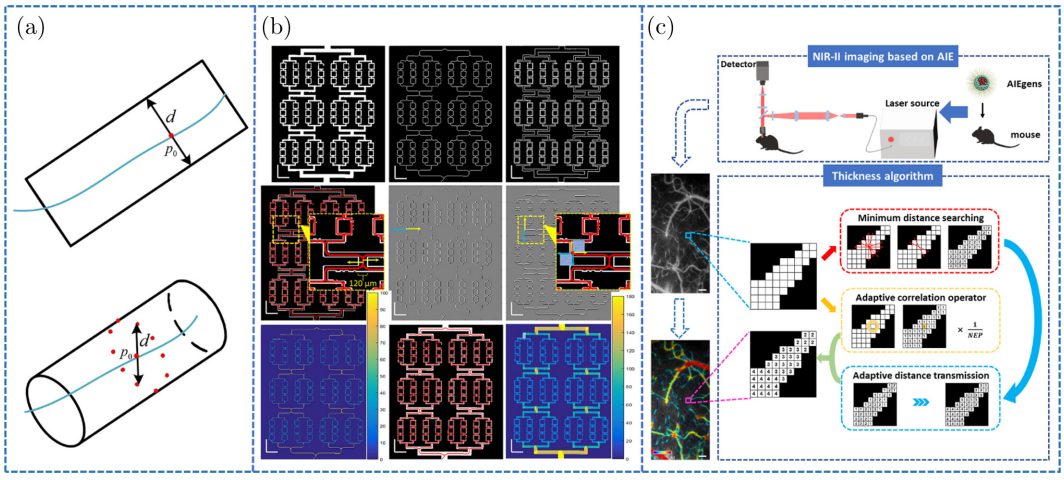

Fig. 7. Schematic representations of thickness quantification methods. (a) Schematic of boundary intersection method in 2D and 3D environments. (b) Flowchart of gradient-guided minimum radial distance thickness quantification method. Scale bar: 0.5 mm. (c) Schematic of automated adaptive windowing-based vessel diameter quantification algorithm. NEP, number of effective pixels. Scale bar: 100 μm. Reproduced with permission from Refs. 81–83.

pixels in the *VPM*, which belongs to the diagonal searching quadrants Q and $\bar{Q}$, respectively. The quantification result was then utilized to generate color-coded diameter maps. Additionally, in order to estimate the mean diameter of all bifurcations within the examined structure, a vessel tracing algorithm was employed.

4.1.3. *Pixel-wise thickness estimation*

Meng *et al.* reported another pixel-wise algorithm to automatically depict the vessel diameter map with high sensitivity, with corresponding schematic shown in Fig. 7(c).[83] The original images were first binarized to create vessel masks. Next, for each vessel pixel in the mask, the minimum distance to the background was calculated, which was followed by an adaptive distance transmission to assign approximately the same distance value to the profile of the vessel. Finally, the adaptive correlation operator was performed to smoothen the image. The quantification result was then pseudo-color coded as the final quantification map.

4.2. *Applications of thickness quantification*

Regarding applications of thickness algorithms, Sun *et al.* compared the 2D and 3D vessel diameter quantification methods in characterizing tumor vascular networks acquired by photoacoustic imaging. As can be seen from probability distributions from 2D and 3D analysis [Fig. 8(a)],[81] the 2D distribution exhibited multiple peaks, while the 3D algorithm improved this deviation by better distinguishing vessels with resemble diameters.[81] However, phantom of vessels distributing outside the optical section might still cause disturbance to the quantification.

Wei *et al.* quantified the thickness of mice cerebral vasculature imaged by optical coherence tomography angiography (OCTA) *in vivo*.[82]

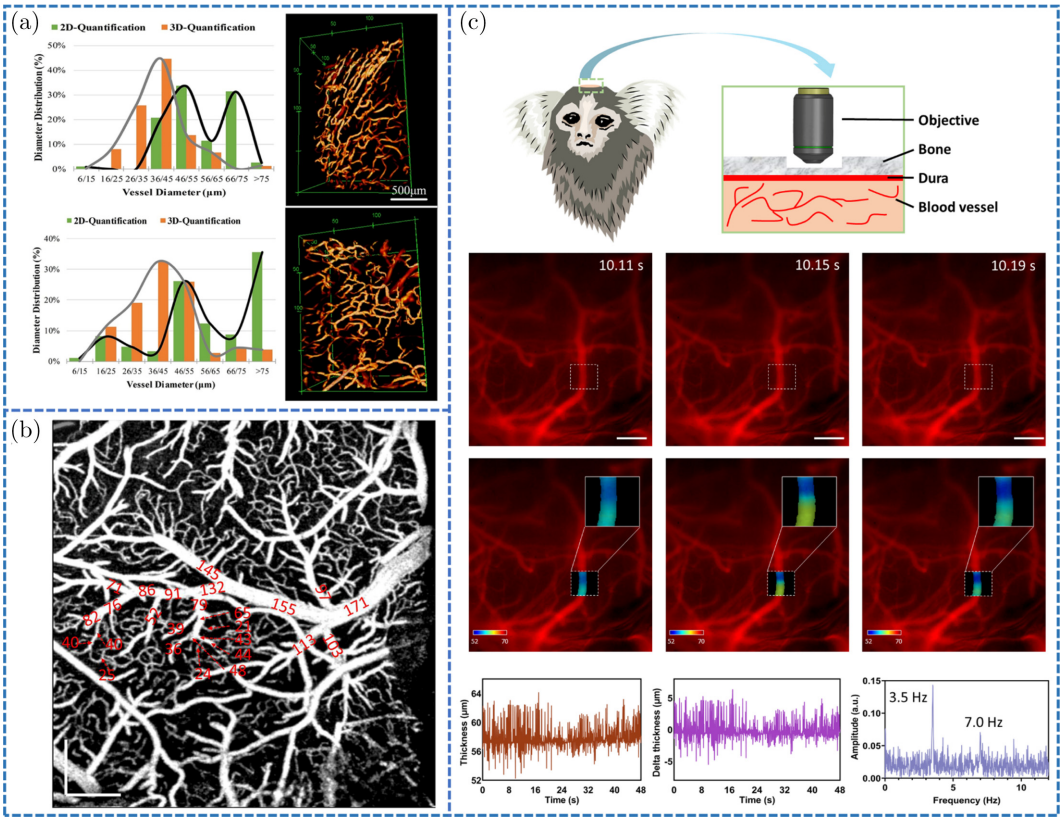

Fig. 8. Application examples of three vessel diameter quantification methods. (a) Vessel diameter histograms extracted by boundary intersection method, along with corresponding 3D renderings. (b) OCTA angiogram with tagged mean vessel diameter values by MRD method combined with vessel tracing algorithm. Scale bar: 0.5 mm. (c) Pixel-wise dynamic monitoring of marmoset cerebral vessel thickness. Reproduced with permission from Refs. 81–83.

Figure 8(b) shows the OCTA image tagged with mean diameter values at local branches calculated by a combination of MRD and vessel tracing. Although this approach offered more detailed results than histogram-based presentations with *in situ* tags with supreme precision and consistency, results were likely to be underestimated at abnormal bloodstream locations and overestimated due to restricted OCT lateral resolution.[82]

Meng *et al.* applied their vessel thickness algorithm to marmoset cerebral blood vessel images.[83] As shown in Fig. 8(c), this algorithm identified dynamic vessel diameter changes as a function of time with high sensitivity. The output pixel-wise thickness map was not only excellent in visualization and accuracy, but also applicable to be adapted to statistical analysis to extract detailed physiological information, such as heartbeat frequency in this case.

5. Discussion and Future Perspective

In summary, we have reviewed various methods to quantify fiber-like structures distribution within biological tissues. These methods are conducted to depict organizational and morphological features of fibrous biological structures from different aspects, including orientation, waviness and thickness. Some methods to quantify fiber orientation distribution also assess fiber alignment degree, which add make-ups to fiber organization quantification. In particular, some new parameters have been defined to describe morphological features of fiber-like structures in detail, such as AI or $A.I.$ ratio, 3D directional variance, *straightness parameter*, *paWav*, and so on.

Early quantitative analysis used the optical FT set-ups to characterize spatial organization of fiber-like structures based on intensity distributions of diffraction patterns.[36,84] The acquired FT spectrum could be further combined with territorial maps to identify orientational feature variations among different imaging locations. However, due to the limited resolution and coarse device, these quantification results were far from intuitive and offered limited assistance in interdisciplinary applications. After the emergence of digital imaging and processing, global features of overall fibrous structures within the image were extracted.[85] With the development of imaging technologies and hardware computational power, subsequent quantification methods improved the characterization precision. Rao *et al.* chose several ROIs and performed FT-SHG analysis on collagen fibers within each ROI.[43] This approach indicated the usefulness of ROI-scale analysis and proved its consistency with the overall fiber alignment. Lau *et al.* further performed gird segmentation before FT analysis on both 2D and 3D images.[55] Each analyzed gridded image was tagged with dark, isotropic or anisotropic according to both signal intensity and FT spectrums, which was somehow similar to that conducted by Rao *et al.*[43] With the generation of a ternary-label map, this method was competent to reflect the orientation distribution with more details. However, the fiber features close to the grid border were likely to be ruptured by the inflexible square grid. Meanwhile, the gird size was another problem since it was critical to the balance of quantification precision and computational time.

By comparison, the pixel-wise quantification method shows advantages in precision for many reasons.[26–28,45,83] First, this method enables pixel-resolved readout of fiber morphological and organization characteristics, making it possible to depict variation of certain features at localized regions within individual fibers. Second, analysis results at each pixel quantitatively and accurately reflect the fiber features in the proximal region which is often referred to as a local window. Depending on the size, this window might not only include other pixels from one single fiber to quantify its morphology, but also include information from neighboring fibers that is required to assess fiber alignment and other collective features. Therefore, the pixel-wise method can naturally overcome the drawbacks of inflexible grid segmentation and global window-based measurement.

Meanwhile, novel algorithms proposed in recent years have also enriched presentation formations, from histograms with curve fittings to pseudo color-coding maps, to achieve a more vivid exhibition of quantification results. Furthermore, quantification techniques with relevant parameters have shown excellent performance in applications of biological structure modeling, carcinoma staging and pathological change recognition, which may enable highly-promising future usage of these newly-developed techniques.

Although there have been independent methods proposed to quantify biological fiber-like structures from distinct perspectives, there seems to be a

naturally developing trend that multi-parametric quantitative analysis is emerging in different application scenarios. For example, both fiber straightness and cross-link density were observed to increase and deemed as collagen signatures in early gastric cancer with lymph node metastasis.[86] Additionally, density and alignment of collagen fibers were found to be significantly higher in grade four renal cell carcinoma than grade one.[87] A combined analysis of orientation, directional variance and waviness was performed in organelle reconstruction recognition, vasculature modeling and pathological change spot identification.[27,28] Moreover, three tumor-associated collagen signatures (TACS) were identified in breast cancer with different collagen density and orientation, indicating that matrix reorganization was relevant to initiation and invasion of breast cancer.[15,88] Later, more TACS were identified to add subdivision in classification of mammary carcinoma progression staging, contributing to establishing a risk prediction model that worked well in prognosis and offered diagnosis and treatment advice.[89]

In the near future, with advances in high-resolution and/or super-resolution microscopy techniques, more methods with improved quantification accuracy shall be highlighted in both researches and clinical applications, serving as robust tools to further investigate biological fibrous structures in exploring and modeling structure-function relationship and pathological development processes.

Acknowledgments

This work was supported by National Key Research and Development Program of China (2019YFE0113700 and 2017YFA0700501), National Natural Science Foundation of China (61905214, 62035011, 11974310 and 31927801), and Natural Science Foundation of Zhejiang Province (LR20F050001).

Conflicts of Interest

The authors declare that there are no conflicts of interest relevant to this article.

References

1. E. Brown, T. McKee, E. diTomaso, A. Pluen, B. Seed, Y. Boucher, R. K. Jain, "Dynamic imaging of collagen and its modulation in tumors in vivo using second-harmonic generation," *Nat Med.* **9**(6), 796–800 (2003).
2. J. Howard, A. A. Hyman, "Dynamics and mechanics of the microtubule plus end," *Nature.* **422**(6933), 753–758 (2003).
3. S. H. Choi, Y. H. Kim, M. Hebisch, C. Sliwinski, S. Lee, C. D'Avanzo, H. C. Chen, B. Hooli, C. Asselin, J. Muffat, J. B. Klee, C. Zhang, B. J. Wainger, M. Peitz, D. M. Kovacs, C. J. Woolf, S. L. Wagner, R. E. Tanzi, D. Y. Kim, "A three-dimensional human neural cell culture model of Alzheimer's disease," *Nature.* **515**(7526), 274-U293 (2014).
4. D. T. Butcher, T. Alliston, V. M. Weaver, "A tense situation: Forcing tumour progression," *Nat. Rev. Cancer.* **9**(2), 108–122 (2009).
5. P. Campagnola, "Second harmonic generation imaging Microscopy: Applications to diseases diagnostics," *Anal. Chem.* **83**(9), 3224–3231 (2011).
6. M. Zhang, M. H. Li, W. T. Zhang, Y. B. Han, Y. H. Zhang, "Simple and efficient delivery of cell-impermeable organic fluorescent probes into live cells for live-cell superresolution imaging," *Light-Sci. Appl.* **8** (2019).
7. M. J. Buehler, "Nature designs tough collagen: Explaining the nanostructure of collagen fibrils," *Proc. Natl. Acad. Sci. U. S. A.* **103**(33), 12285–90 (2006).
8. C. P. Lin, M. Schuster, S. C. Guimaraes, P. Ashwin, M. Schrader, J. Metz, C. Hacker, S. J. Gurr, G. Steinberg, "Active diffusion and microtubule-based transport oppose myosin forces to position organelles in cells," *Nat. Commun.* **7** (2016).
9. A. Weber, J. I. Turri, R. Benitez, S. Zemljic-Jokhadar, J. L. T. Oca-Herrera, "Microtubule disruption changes endothelial cell mechanics and adhesion," *Sci. Rep-Uk.* **9**, (2019).
10. G. Ehrenstein, H. Lecar, "Mechanism of signal transmission in nerve axons," *Annu. Rev. Biophys. Bio.* **1**, 347–368 (1972).
11. L. Wan, J. Skoko, J. Yu, O. B. Ozdoganlar, P. R. LeDuc, C. A. Neumann, "Mimicking embedded vasculature structure for 3D cancer on a chip approaches through micromilling (vol 7, 16724, 2017)," *Sci. Rep-Uk.* **9** (2019).
12. K. M. Yamada, "Cell-surface interactions with extracellular materials," *Annu. Rev. Biochem.* **52**, 761–799 (1983).
13. M. Aumailley, B. Gayraud, "Structure and biological activity of the extracellular matrix," *J. Mol. Med.-Jmm.* **76**(3–4), 253–265 (1998).
14. K. P. Quinn, K. E. Sullivan, Z. Y. Liu, Z. Ballard, C. Siokatas, I. Georgakoudi, L. D. Black, "Optical metrics of the extracellular matrix predict

compositional and mechanical changes after myocardial infarction," *Sci. Rep.-Uk.* **6** (2016).
15. P. P. Provenzano, K. W. Eliceiri, J. M. Campbell, D. R. Inman, J. G. White, P. J. Keely, "Collagen reorganization at the tumor-stromal interface facilitates local invasion," *Bmc Med.* **4** (2006).
16. P. J. Campagnola, C. Y. Dong, "Second harmonic generation microscopy: Principles and applications to disease diagnosis," *Laser Photonics Rev.* **5**(1), 13–26 (2011).
17. S. Bancelin, A. Nazac, B. H. Ibrahim, P. Dokladal, E. Decenciere, B. Teig, H. Haddad, H. Fernandez, M. C. Schanne-Klein, A. De Martino, "Determination of collagen fiber orientation in histological slides using Mueller microscopy and validation by second harmonic generation imaging," *Opt. Express.* **22**(19), 22561–22574 (2014).
18. M. P. Rubbens, A. Driessen-Mol, R. A. Boerboom, M. M. J. Koppert, H. C. van Assen, B. M. T. Romeny, F. P. T. Baaijens, C. V. C. Bouten, "Quantification of the temporal evolution of collagen orientation in mechanically conditioned engineered cardiovascular tissues," *Ann. Biomed. Eng.* **37**(7), 1263–1272 (2009).
19. J. Wu, B. Rajwa, D. L. Filmer, C. M. Hoffmann, B. Yuan, C. S. Chiang, J. Sturgis, J. P. Robinson, "Analysis of orientations of collagen fibers by novel fiber-tracking software," *Microsc. Microanal.* **9**(6), 574–580 (2003).
20. P. J. Campagnola, L. M. Loew, "Second-harmonic imaging microscopy for visualizing biomolecular arrays in cells, tissues and organisms," *Nat. Biotechnol.* **21**(11), 1356–1360 (2003).
21. W. R. Zipfel, R. M. Williams, W. W. Webb, "Nonlinear magic: Multiphoton microscopy in the biosciences," *Nat. Biotechnol.* **21**(11), 1368–1376 (2003).
22. M. Sivaguru, S. Durgam, R. Ambekar, D. Luedtke, G. Fried, A. Stewart, K. C. Toussaint, "Quantitative analysis of collagen fiber organization in injured tendons using Fourier transform-second harmonic generation imaging," *Opt. Express.* **18**(24), 24983–24993 (2010).
23. R. Ambekar, M. Chittenden, I. Jasiuk, K. C. Toussaint, "Quantitative second-harmonic generation microscopy for imaging porcine cortical bone: Comparison to SEM and its potential to investigate age-related changes," *Bone.* **50**(3), 643–650 (2012).
24. R. Y. Wang, L. P. Brewster, R. L. Gleason, "*In-situ* characterization of the uncrimping process of arterial collagen fibers using two-photon confocal microscopy and digital image correlation," *J. Biomech.* **46**(15), 2726–2729 (2013).
25. M. Winkler, G. Shoa, Y. L. Xie, S. J. Petsche, P. M. Pinsky, T. Juhasz, D. J. Brown, J. V. Jester, "Three-dimensional distribution of transverse collagen fibers in the anterior human corneal stroma," *Invest. Ophth. Vis. Sci.* **54**(12), 7293–7301 (2013).
26. Z. Y. Liu, D. Pouli, D. Sood, A. Sundarakrishnan, C. K. H. Mingalone, L. M. Arendt, C. Alonzo, K. P. Quinn, C. Kuperwasser, L. Zeng, T. Schnelldorfer, D. L. Kaplan, I. Georgakoudi, "Automated quantification of three-dimensional organization of fiber-like structures in biological tissues," *Biomaterials.* **116**, 34–47 (2017).
27. S. H. Qian, J. Meng, W. J. Liu, C. C. Wang, R. S. Jiang, L. Yang, X. Liu, C. F. Kuang, Z. H. Ding, Z. Y. Liu, "Identification of endoplasmic reticulum formation mechanism by multi-parametric, quantitative super-resolution imaging," *Opt. Lett.* **47**(2), 357–360 (2022).
28. S. H. Qian, J. Meng, Z. Feng, L. X. Zhou, S. Y. Jiang, Y. L. Wang, Z. T. Ye, S. M. Zhuo, J. X. Chen, X. J. Li, L. X. Gao, Z. H. Ding, J. Qian, Z. Y. Liu, "Mapping organizational changes of fiber-like structures in disease progression by multi-parametric, quantitative imaging," *Laser Photonics Rev.* **16**(6) (2022).
29. S. Thomopoulos, J. P. Marquez, B. Weinberger, V. Birman, G. M. Genin, "Collagen fiber orientation at the tendon to bone insertion and its influence on stress concentrations," *J. Biomech.* **39**(10), 1842–1851 (2006).
30. M. Hadian, B. M. Corcoran, R. I. Han, J. G. Grossmann, J. P. Bradshaw, "Collagen organization in canine myxomatous mitral valve disease: An X-ray diffraction study," *Biophys. J.* **93**(7), 2472–2476 (2007).
31. P. S. Robinson, R. T. Tranquillo, "Planar biaxial behavior of fibrin-based tissue-engineered heart valve leaflets," *Tissue Eng. Pt. A.* **15**(10), 2763–2772 (2009).
32. C. Bayan, J. M. Levitt, E. Miller, D. Kaplan, I. Georgakoudi, "Fully automated, quantitative, noninvasive assessment of collagen fiber content and organization in thick collagen gels," *J. Appl. Phys.* **105**(10) (2009).
33. K. P. Quinn, A. Golberg, G. F. Broelsch, S. Khan, M. Villiger, B. Bouma, W. G. Austen, R. L. Sheridan, M. C. Mihm, M. L. Yarmush, I. Georgakoudi, "An automated image processing method to quantify collagen fibre organization within cutaneous scar tissue," *Exp. Dermatol.* **24**(1), 78–80 (2015).
34. E. Hase, T. Minamikawa, K. Sato, D. Yonekura, M. Takahashi, T. Yasui, "Quantitative evaluation of both histological and mechanical recovery in injured tendons using fourier-transform second-harmonic-generation microscopy," *Ieee J. Sel. Top. Quant.* **27**(4) (2021).

35. S. L. Lee, Y. F. Chen, C. Y. Dong, "Probing multiscale collagenous tissue by nonlinear microscopy," *Acs Biomater. Sci. Eng.* **3**(11), 2825–2831 (2017).
36. A. Dziedzicgoclawska, M. Rozycka, J. C. Czyba, W. Sawicki, R. Moutier, S. Lenczowski, K. Ostrowski, "Application of the optical fourier-transform for analysis of the spatial-distribution of collagen-fibers in normal and osteopetrotic bone tissue," *Histochemistry.* **74**(1), 123–137 (1982).
37. R. A. R. Rao, M. R. Mehta, S. Leithem, K. C. Toussaint, "Quantitative analysis of forward and backward second-harmonic images of collagen fibers using Fourier transform second-harmonic-generation microscopy," *Opt. Lett.* **34**(24), 3779–3781 (2009).
38. Y. J. Zhou, Y. P. Zheng, "Estimation of muscle fiber orientation in ultrasound images using revoting Hough transform (RVHT)," *Ultrasound. Med. Biol.* **34**(9), 1474–1481 (2008).
39. W. J. Karlon, P. P. Hsu, S. Li, S. Chien, A. D. McCulloch, J. H. Omens, "Measurement of orientation and distribution of cellular alignment and cytoskeletal organization," *Ann. Biomed. Eng.* **27** (6), 712–720 (1999).
40. F. Daniels, B. M. ter Haar Romeny, M. Rubbens, H. van Assen, "Quantification of collagen orientation in 3D engineered tissue," *Ifmbe Proc.* **15**, 282–+ (2007).
41. Z. Y. Liu, L. Speroni, K. P. Quinn, C. Alonzo, D. Pouli, Y. Zhang, E. Stuntz, C. Sonnenschein, A. M. Soto, I. Georgakoudi, "3D organizational mapping of collagen fibers elucidates matrix remodeling in a hormone-sensitive 3D breast tissue model," *Biomaterials.* **179**, 96–108 (2018).
42. V. Ayyalasomayajula, B. Pierrat, P. Badel, "A computational model for understanding the micromechanics of collagen fiber network in the tunica adventitia," *Biomechanics and Modeling in Mechanobiology.* **18**(5), 1507–1528 (2019).
43. R. A. R. Rao, M. R. Mehta, K. C. Toussaint, "Fourier transform-second-harmonic generation imaging of biological tissues," *Opt. Express.* **17**(17), 14534–14542 (2009).
44. K. P. Quinn, I. Georgakoudi, "Rapid quantification of pixel-wise fiber orientation data in micrographs," *J. Biomed. Opt.* **18**(4) (2013).
45. Z. Liu, K. P. Quinn, L. Speroni, L. Arendt, C. Kuperwasser, C. Sonnenschein, A. M. Soto, I. Georgakoudi, "Rapid three-dimensional quantification of voxel-wise collagen fiber orientation," *Biomed. Opt. Express.* **6**(7), 2294–310 (2015).
46. S. Mori, J. Y. Zhang, "Principles of diffusion tensor imaging and its applications to basic neuroscience research," *Neuron.* **51**(5), 527–539 (2006).
47. T. E. Conturo, N. F. Lori, T. S. Cull, E. Akbudak, A. Z. Snyder, J. S. Shimony, R. C. McKinstry, H. Burton, M. E. Raichle, "Tracking neuronal fiber pathways in the living human brain," *P. Natl. Acad. Sci. USA.* **96**(18), 10422–10427 (1999).
48. P. J. Basser, J. Mattiello, D. Lebihan, "Mr diffusion tensor spectroscopy and imaging," *Biophys. J.* **66**(1), 259–267 (1994).
49. A. Markus, K. Amunts, D. Grassel, C. Palm, J. Dammers, H. Axer, U. Pietrzyk, K. Zilles, "A novel approach to the human connectome: Ultra-high resolution mapping of fiber tracts in the brain," *Neuroimage.* **54**(2), 1091–1101 (2011).
50. J. S. Bredfeldt, Y. M. Liu, C. A. Pehlke, M. W. Conklin, J. M. Szulczewski, D. R. Inman, P. J. Keely, R. D. Nowak, T. R. Mackie, K. W. Eliceiri, "Computational segmentation of collagen fibers from second-harmonic generation images of breast cancer," *J. Biomed. Opt.* **19**(1) (2014).
51. A. M. Stein, D. A. Vader, L. M. Jawerth, D. A. Weitz, L. M. Sander, "An algorithm for extracting the network geometry of three-dimensional collagen gels," *J. Microsc.-Oxford.* **232**(3), 463–475 (2008).
52. C. Venter, C. U. Niesler, "Cellular alignment and fusion: Quantifying the effect of macrophages and fibroblasts on myoblast terminal differentiation," *Exp. Cell. Res.* **370**(2), 542–550 (2018).
53. F. Xu, T. Beyazoglu, E. Hefner, U. A. Gurkan, U. Demirci, "Automated and adaptable quantification of cellular alignment from microscopic images for tissue engineering applications," *Tissue. Eng. Part C Methods.* **17**(6), 641–9 (2011).
54. R. Ambekar, T. Y. Lau, M. Walsh, R. Bhargava, K. C. Toussaint, "Quantifying collagen structure in breast biopsies using second-harmonic generation imaging," *Biomedical Optics Express.* **3**(9), 2021–2035 (2012).
55. T. Y. Lau, H. K. Sangha, E. K. Chien, B. L. McFarlin, A. J. Wagoner Johnson, K. C. Toussaint, Jr., "Application of Fourier transform-second-harmonic generation imaging to the rat cervix," *J. Microsc.* **251**(1), 77–83 (2013).
56. T. Y. Lau, R. Ambekar, K. C. Toussaint, "Quantification of collagen fiber organization using three-dimensional Fourier transform-second-harmonic generation imaging," *Opt. Express.* **20** (19), 21821–21832 (2012).
57. F. Rodriguez-Pascual, D. A. Slatter, "Collagen cross-linking: Insights on the evolution of metazoan extracellular matrix," *Sci. Rep.-Uk.* **6** (2016).
58. M. Huang, Z. Liu, L. Baugh, J. DeFuria, A. Maione, A. Smith, O. Kashpur, L. D. Black Iii, I. Georgakoudi, M. L. Whitfield, J. Garlick, "Lysyl oxidase enzymes mediate TGF-beta1-induced fibrotic

phenotypes in human skin-like tissues," *Lab. Invest.* **99**(4), 514–527 (2019).
59. V. Lutz, M. Sattler, S. Gallinat, H. Wenck, R. Poertner, F. Fischer, "Impact of collagen crosslinking on the second harmonic generation signal and the fluorescence lifetime of collagen autofluorescence," *Skin Res. Technol.* **18**(2), 168–179 (2012).
60. J. E. Marturano, J. F. Xylas, G. V. Sridharan, I. Georgakoudi, C. K. Kuo, "Lysyl oxidase-mediated collagen crosslinks may be assessed as markers of functional properties of tendon tissue formation," *Acta. Biomater.* **10**(3), 1370–1379 (2014).
61. R. Rezakhaniha, A. Agianniotis, J. T. C. Schrauwen, A. Griffa, D. Sage, C. V. C. Bouten, F. N. van de Vosse, M. Unser, N. Stergiopulos, "Experimental investigation of collagen waviness and orientation in the arterial adventitia using confocal laser scanning microscopy," *Biomechanics and Modeling in Mechanobiology.* **11**(3–4), 461–473 (2012).
62. S. Zeinali-Davarani, Y. J. Wang, M. J. Chow, R. Turcotte, Y. H. Zhang, "Contribution of collagen fiber undulation to regional biomechanical properties along porcine thoracic aorta," *J. Biomech. Eng.-T Asme.* **137**(5) (2015).
63. J. Concannon, J. P. McGarry, "Development of an FEA framework for analysis of subject-specific aortic compliance based on 4D flow MRI," *Acta Biomater.* **125**, 154–171 (2021).
64. B. Fata, C. A. Carruthers, G. Gibson, S. C. Watkins, D. Gottlieb, J. E. Mayer, M. S. Sacks, "Regional structural and biomechanical alterations of the ovine main pulmonary artery during postnatal growth," *J. Biomech. Eng.-T Asme.* **135**(2) (2013).
65. A. Tamura, Y. Kato, K. Matsumoto, "Modeling elastic lamina buckling in the unloaded aortic media," *Mech. Eng. J.* **8**(1) (2021).
66. B. Jones, J. R. Tonniges, A. Debski, B. Albert, D. A. Yeung, N. Gadde, A. Mahajan, N. Sharma, E. P. Calomeni, M. R. Go, C. P. Hans, G. Agarwal, "Collagen fibril abnormalities in human and mice abdominal aortic aneurysm," *Acta. Biomater.* **110**, 129–140 (2020).
67. F. Benboujja, C. S. Hartnick, "Quantitative evaluation of the human vocal fold extracellular matrix using multiphoton microscopy and optical coherence tomography," *Sci. Rep.-Uk.* **11**(1) (2021).
68. S. K. Chakrapani, V. Dayal, D. Barnard, "Detection and characterization of waviness in unidirectional Gfrp using rayleigh wave air coupled ultrasonic testing (Rac-Ut)," *Res. Nondestruct. Eval.* **24**(4), 191–201 (2013).
69. M. J. Chow, R. Turcotte, C. P. Lin, Y. H. Zhang, "Arterial extracellular matrix: A mechanobiological study of the contributions and interactions of elastin and collagen," *Biophys. J.* **106**(12), 2684–2692 (2014).
70. R. H. Cox, "Passive mechanics and connective-tissue composition of canine arteries," *Am. J. Physiol.* **234**(5), H533-H541 (1978).
71. H. Chen, M. N. Slipchenko, Y. Liu, X. F. Zhao, J. X. Cheng, Y. Lanir, G. S. Kassab, "Biaxial deformation of collagen and elastin fibers in coronary adventitia," *J. Appl. Physiol.* **115**(11), 1683–1693 (2013).
72. C. Y. Li, S. Shan, Q. Huang, R. D. Braun, J. Lanzen, K. Hu, P. Lin, M. W. Dewhirst, "Initial stages of tumor cell-induced angiogenesis: Evaluation via skin window chambers in rodent models," *J. Natl. Cancer Inst.* **92**(2), 143–7 (2000).
73. D. A. Greenberg, K. Jin, "From angiogenesis to neuropathology," *Nature.* **438**(7070), 954–9 (2005).
74. S. Kochli, K. Endes, D. Infanger, L. Zahner, H. Hanssen, "Obesity, blood pressure, and retinal vessels: A meta-analysis," *Pediatrics.* **141**(6) (2018).
75. L. An, H. M. Subhush, D. J. Wilson, R. K. Wang, "High-resolution wide-field imaging of retinal and choroidal blood perfusion with optical microangiography," *J. Biomed. Opt.* **15**(2), 026011 (2010).
76. S. Abdullateef, J. Mariscal-Harana, A. W. Khir, "Impact of tapering of arterial vessels on blood pressure, pulse wave velocity, and wave intensity analysis using one-dimensional computational model," *Int. J. Numer Method Biomed. Eng.* **37**(11), e3312 (2021).
77. S. Kochli, K. Endes, R. Steiner, L. Engler, D. Infanger, A. Schmidt-Trucksass, L. Zahner, H. Hanssen, "Obesity, high blood pressure, and physical activity determine vascular phenotype in young children," *Hypertension.* **73**(1), 153–161 (2019).
78. K. Imhof, L. Zahner, A. Schmidt-Trucksass, H. Hanssen, "Association of body composition and blood pressure categories with retinal vessel diameters in primary school children," *Hypertens. Res.* **39**(6), 423–9 (2016).
79. B. Gopinath, J. J. Wang, A. Kifley, A. G. Tan, T. Y. Wong, P. Mitchell, "Influence of blood pressure and body mass index on retinal vascular caliber in preschool-aged children," *J. Hum. Hypertens.* **27**(9), 523–8 (2013).
80. P. Mitchell, N. Cheung, K. de Haseth, B. Taylor, E. Rochtchina, F. M. Islam, J. J. Wang, S. M. Saw, T. Y. Wong, "Blood pressure and retinal arteriolar

narrowing in children," *Hypertension.* **49**(5), 1156–62 (2007).

81. M. Sun, C. Li, N. Chen, H. Zhao, L. Ma, C. Liu, Y. Shen, R. Lin, X. Gong, "Full three-dimensional segmentation and quantification of tumor vessels for photoacoustic images," *Photoacoustics.* **20**, 100212 (2020).
82. W. Wei, Q. Zhang, S. G. Rayner, W. Qin, Y. Cheng, F. Wang, Y. Zheng, R. K. Wang, "Automated vessel diameter quantification and vessel tracing for OCT angiography," *J. Biophotonics.* **13**(12), e202000248 (2020).
83. J. Meng, Z. Feng, S. H. Qian, C. C. Wang, X. J. Li, L. X. Gao, Z. H. Ding, J. Qian, Z. Y. Liu, "Mapping physiological and pathological functions of cortical vasculature through aggregation-induced emission nanoprobes assisted quantitative, in vivo NIR-II imaging," *Biomater Adv.* **136** (2022).
84. S. Lenczowski, M. Rozycka, W. Sawicki, M. Daszkiewicz, W. Baranska, A. Dziedzic-Goclawska, K. Ostrowski, "Microscopic image analysis by the optical Fourier transform," *Mater. Med. Pol.* **12**(4), 272–85 (1980).
85. J. Smolle, M. Fiebiger, R. Hofmann-Wellenhof, H. Kerl, "Quantitative morphology of collagen fibers in cutaneous malignant melanoma and melanocytic nevus," *Am. J. Dermatopathol.* **18**(4), 358–63 (1996).
86. D. X. Chen, G. Chen, W. Jiang, M. T. Fu, W. J. Liu, J. Sui, S. Y. Xu, Z. Y. Z. Liu, X. L. Zheng, L. J. Chi, D. J. Lin, K. Li, W. S. Chen, N. Zuo, J. P. Lu, J. X. Chen, G. X. Li, S. M. Zhuo, J. Yan, "Association of the collagen signature in the tumor microenvironment with lymph node metastasis in early gastric cancer," *Jama. Surg.* **154**(3) (2019).
87. S. L. Best, Y. M. Liu, A. Keikhosravi, C. R. Drifka, K. M. Woo, G. S. Mehta, M. Altwegg, T. N. Thimm, M. Houlihan, J. S. Bredfeldt, E. J. Abel, W. Huang, K. W. Eliceiri, "Collagen organization of renal cell carcinoma differs between low and high grade tumors," *Bmc Cancer.* **19** (2019).
88. P. P. Provenzano, D. R. Inman, K. W. Eliceiri, J. G. Knittel, L. Yan, C. T. Rueden, J. G. White, P. J. Keely, "Collagen density promotes mammary tumor initiation and progression," *Bmc Med.* **6**, 11 (2008).
89. G. Q. Xi, W. H. Guo, D. Y. Kang, J. L. Ma, F. M. Fug, L. D. Qiu, L. Q. Zheng, J. J. He, N. Fang, J. H. Chen, J. T. Li, S. M. Zhuo, X. X. Liao, H. H. Tun, L. H. Li, Q. Y. Zhang, C. Wang, S. A. Boppart, J. X. Chen, "Large-scale tumor-associated collagen signatures identify high-risk breast cancer patients," *Theranostics.* **11**(7), 3229–3243 (2021).